



Published in final edited form as:

ACS Nano. 2017 February 28; 11(2): 1466–1477. doi:10.1021/acsnano.6b06777.

Highly Specific and Sensitive Fluorescent Nanoprobes for Image-Guided Resection of Sub-Millimeter Peritoneal Tumors

Aaron H. Colby^{†,‡,⊥}, Samantha M. Berry^{†,⊥}, Ann M. Moran[§], Kristine Amber Pasion[§], Rong Liu[†], Yolonda L. Colson[‡], Nelson Ruiz-Opazo[§], Mark W. Grinstaff^{†,§,*}, and Victoria L. M. Herrera^{§,*}

[†]Departments of Biomedical Engineering and Chemistry, Boston University, Boston, Massachusetts 02215, United States

[‡]Division of Thoracic Surgery, Department of Surgery, Brigham and Women's Hospital, Boston, Massachusetts 02115, United States

[§]Department of Medicine and Whitaker Cardiovascular Institute, Boston University School of Medicine, Boston, Massachusetts 02118, United States

Abstract

A current challenge in the treatment of peritoneal carcinomatosis is the inability to detect, visualize, and resect small or microscopic tumors of pancreatic, ovarian, or mesothelial origin. In these diseases, the completeness of primary tumor resection is directly correlated with patient survival, and hence, identifying small sub-millimeter tumors (*i.e.*, disseminated disease) is critical. Thus, new imaging techniques and probes are needed to improve cytoreductive surgery and patient outcomes. Highly fluorescent rhodamine-labeled expansile nanoparticles (HFR-eNPs) are described for use as a visual aid during cytoreductive surgery of pancreatic carcinomatosis. The covalent incorporation of rhodamine into ~30 nm eNPs increases the fluorescent signal compared to free rhodamine, thereby affording a brighter and more effective probe than would be achieved by a single rhodamine molecule. Using the intraperitoneal route of administration, HFR-eNPs localize to regions of large (~1 cm), sub-centimeter, and sub-millimeter intraperitoneal tumor in three different animal models, including pancreatic, mesothelioma, and ovarian carcinoma. Tumoral localization of the HFR-eNPs depends on both the material property (*i.e.*, eNP polymer)

*Corresponding Authors: mgrin@bu.edu, vherrera@bu.edu.

⊥ Author Contributions

A.H.C. and S.B. contributed equally to the work.

ORCID

Mark W. Grinstaff: 0000-0002-5453-3668

Author Contributions

The manuscript was written by A.H.C., V.L.M.H., S.B., N.R.O., and M.W.G. The experiments were conducted by V.L.M.H., A.H.C., S.B., A.M.M., K.A.P., and R.L.

Notes

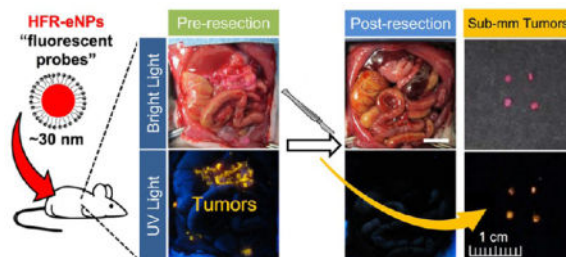
The authors declare the following competing financial interest(s): MWG and AHC are co-founders of a start-up company (Ionic Pharmaceuticals) evaluating the technology.

Supporting Information

The Supporting Information is available free of charge on the ACS Publications website at DOI: 10.1021/acsnano.6b06777. Comparison of *ex vivo* fluorescence of 0.2% HFR-eNPs and 2% HFR-eNPs (Figure S1); panels of bright light and UV light images of normal tissues (Figures S2 and S3) and tumor tissues (Figure S4) from two additional animals that underwent HFR-eNP-guided resections; Figure S5 shows pre- and post-resection *in situ* and *ex vivo* images from these same animals (PDF)

as well as the surface chemistry (anionic surfactant vs PEGylated noncharged surfactant). In a rat model of pancreatic carcinomatosis, HFR-eNP identification of tumor is validated against gold-standard histopathological analysis to reveal that HFR-eNPs possess high specificity (99%) and sensitivity (92%) for tumors, in particular, sub-centimeter and microscopic sub-millimeter tumors, with an overall accuracy of 95%. Finally, as a proof-of-concept, HFR-eNPs are used to guide the resection of pancreatic tumors in a rat model of peritoneal carcinomatosis.

Graphical Abstract



Keywords

fluorescently guided resection; pancreatic cancer; peritoneal carcinomatosis; fluorescent nanoparticle probes; expansile nanoparticles

Molecular, macromolecular, and nanoparticulate optical imaging probes are of significant scientific and clinical interest for the identification of tumors in the surgical setting. These technologies address a major unmet clinical need: the inability to visualize and resect microscopic peritoneal tumors. Recent advances in optical imaging probes for clinical applications have produced a plethora of technologies, including single-walled carbon nanotubes,¹ antibody (Ab)-conjugated fluorescent dyes,^{2,3} Ab-conjugated positron emission tomography (PET) immunoconjugates,⁴ near-infrared (NIR) indocyanine green/albumin supramolecular complexes^{5,6} or loaded-nanoparticles,⁷ NIR fluorescent dyes that are quenched and only emit upon exposure to protease activity or separation from the antibody,⁸ folic-acid-conjugated NIR fluorescent dyes,^{9,10} nanoprobe that use the second NIR window (NIR-II),¹¹ NIR quantum dots coated with cyclic Arg-Gly-Asp peptides,^{12,13} palladium nanosheets for photoacoustic imaging,¹⁴ and fluorescently labeled pH (low) insertion peptides (pHLIPs).¹⁵

Several of these technologies are being developed to enhance intraoperative optical imaging and identification of peritoneal carcinomatosis which arises from gynecologic and gastrointestinal malignancies such as ovarian, mesothelioma, pancreatic, colorectal, and gastric carcinomas. Peritoneal carcinomatosis is characterized by asymptomatic onset with rapid disease progression, wherein peritoneal tumors invade the bowel wall causing gut erosion, fistula formation, intractable abdominal pain, bowel dysfunction, as well as debilitating ascites and cachexia. Current treatment approaches are palliative cytoreductive/debulking surgery to relieve symptomatic obstruction followed by administration of systemic chemotherapy for ovarian, gastric, mesothelial, and colorectal peritoneal carcinomatosis.^{16,17} In marked contrast, for peritoneal carcinomatosis of pancreatic ductal

adenocarcinoma origin (PDAC-PC; *i.e.*, tumor that originated in the pancreas but has disseminated throughout the peritoneum), cytoreductive/debulking surgery is not as effective. This is surprising in light of the direct relationship between the completeness of primary PDAC resection and patient survival.^{18,19} Feed-forward cycles of dissemination and progression in PDAC-PC^{20,21} and a low, 20% 5-year survival rate compared to other peritoneal carcinomatoses^{22–24} suggest that significant residual sub-millimeter or occult peritoneal tumors remain following PDAC-PC resections.

To improve outcomes in cytoreductive surgery and, in particular, PDAC-PC, “visual assists” are being investigated to address the difficulty of visualizing sub-millimeter occult disease, which is often the most difficult to identify and resect. For example, PET/CT imaging of tumors has been found to be more sensitive than CT alone, but this technique cannot detect sub-centimeter tumors and certainly not sub-millimeter tumors.²⁵ Thus, a current limitation in treatment is the inability to detect, and hence surgically remove, sub-millimeter peritoneal tumors. Improving surgeons’ ability to detect these small tumors intraoperatively presents the opportunity to achieve more complete cytoreductive surgery and, potentially, increase progression-free and overall survival.

While the aforementioned optical probes exhibit probe-specific advantages with several used in the clinic, and two even FDA-approved (indocyanine green by Diagnostic Green GmbH and methylene blue (ProveDye) by Provepharm SAS), probe performance improvement remains a need, especially for PDAC-PC. For example, fluorescently labeled antibodies require the use of different antibodies for each tumor subtype. This approach is therefore not broadly applicable across different tumor types and inpatient tumor heterogeneity. NIR dyes have limited background autofluorescence and do not suffer from the obstacle of limited light penetration through tissue as occurs with fluorescent probes. However, NIR-imaging requires expensive capital equipment, complicated instruments, and video, which present logistical hurdles in the sterile intraoperative field.^{26,27} Moreover, fluorescently conjugated small molecules, peptides, or antibodies generally possess one fluorophore per probe and, thus, limited sensitivity; these probes also suffer from accumulation in normal tissues, such as the kidney. Finally, nanotechnology-based probes suffer from limited accumulation in tumor tissue after intravenous injection.²⁸

Building on our observation that expansile nanoparticles (eNPs) localize to peritoneal tumors after intraperitoneal (IP) injection,^{29–32} we are developing highly fluorescent, rhodamine-labeled expansile nanoparticles (HFR-eNPs) as nanoprobe to assist in the visualization and resection of intraperitoneal tumors that are not detectable *via* current clinical imaging modalities (*i.e.*, sub-centimeter tumors) or by the surgeon intraoperatively (*i.e.*, sub-millimeter tumors) in three different human tumor models of intraperitoneal carcinomatosis of mesothelial, ovarian, and pancreatic origin. Herein, we report the (1) synthesis of HFR-eNPs with varying incorporations of conjugated rhodamine; (2) amplification of rhodamine fluorescence *via* loading in the HFR-eNPs; (3) facile visualization *via* an inexpensive, hand-held UV lamp of HFR-eNP localization to mesothelial (MSTO-211H), ovarian (OVCAR-3), and pancreatic (Panc1 cancer stem cell; Panc1-CSC) peritoneal tumors following intraperitoneal injection; (4) impact of nanoparticle surface charge and expansile property on localization; (5) specificity and sensitivity of HFR-

eNP localization to PDAC-PC tumors while sparing adjacent normal mesothelium, microvasculature, and organs; (6) HFR-eNP localization to sub-millimeter peritoneal tumors; (7) localization of HFR-eNPs to tumor cell clusters with high expression of lactate dehydrogenase-A (LDH-A); and (8) proof-of-principle, intraoperative image-guided resection of sub-millimeter pancreatic tumors in a PDAC-PC xenograft rat model.

RESULTS AND DISCUSSION

HFR-eNPs were synthesized following a published procedure³² and evaluated for particle diameter, surface charge, and fluorescence. Rhodamine methyl methacrylate was covalently incorporated into the polymer backbone at 0.02, 0.2, and 2 % wt/wt (rhodamine/polymer) to yield particles with differing fluorescence properties. Increasing rhodamine loading did not significantly impact HFR-eNP diameter, as determined by scanning electron microscopy (SEM), with all formulations having a mean diameter of ~30 nm (Figure 1a,b). However, characterization *via* dynamic light scattering (DLS) suggested a mean diameter of >200 nm for all particles with a significantly larger average diameter (~360 nm) for the 2% HRF-eNPs (Figure 1a,c). The disparity in results between these two methods are in agreement with previous reports^{31,32} and are attributed to the bias toward a low number of larger (100–400 nm) nanoparticles that skew DLS results. An in-depth discussion of the factors that lead to DLS bias toward larger particles (*i.e.*, the Rayleigh approximation) is detailed in Eldridge *et al.*³³ All HFR-eNPs exhibited a negative ζ -potential between –36.9 and –45.5 mV and, by SEM, a smooth, spherical morphology (Figure 1b). HFR-eNPs demonstrated negligible cytotoxicity *in vitro* below concentrations of 37 $\mu\text{g}/\text{mL}$, similar to previously reported eNP formulations (Figure 1d).^{29,31,34–36}

To estimate the rhodamine incorporation per particle, the density of the eNP polymer was measured by rehydrating a lyophilized sample using a volumetric flask. Using the density, 1.26 g/mL, in combination with the average particle diameter by SEM, we estimate the incorporation of rhodamine fluorophores per 30 nm HFR-eNP particle to be ~3, ~31, and ~314 in 0.02, 0.2, and 2.0 % wt/wt HRF-eNPs, respectively. Increasing rhodamine loading 10-fold from 0.02 to 0.2 % wt/wt resulted in significant optical differences in the particles and a nearly linear 8.3-fold increase in area under the curve (AUC) of the fluorescence emission spectrum from 565 to 700 nm (Figure 1e, inset). However, a further 10-fold increase in rhodamine from 0.2 to 2 % wt/wt only resulted in a 1.5-fold increase in AUC, indicating that at this higher loading there is significant self-quenching of the rhodamine. Interestingly, the fluorescence intensity/AUC for 0.02 and 0.2% HFR-eNPs is significantly greater than that of equivalent concentrations of free rhodamine (Figure 1e). Fluorescence enhancement of fluorophores embedded within a solid matrix as compared to free solution has been shown before within poly(methyl methacrylate) (PMMA) matrices as well as with silica particles.^{37–39} Increased fluorescence in the PMMA particles was attributed to a decrease in the nonradiative rate constant of the fluorophore, which was affected by the increased viscosity and decreased polarity of the PMMA environment *versus* water. Similarly, it has been reported that rhodamine B possesses increased quantum efficiency with increased viscosity and decreased polarity of its environment, thereby corroborating the current results.⁴⁰ Interestingly, PLGA-NPs covalently labeled with rhodamine do not produce a significant increase in fluorescence compared to free rhodamine (Figure 1e). This

may be due to the increased mobility of the PLGA chains compared to eNPs and/or a less hydrophobic local environment. The 0.2 % wt/wt rhodamine formulation was chosen for subsequent *in vivo* studies because of its balance between high fluorescent efficiency (Figure 1e) and overall fluorescence per mass of polymer, which was similar to the 2% HFR-eNPs (Figure 1f).

HFR-eNP tumor localization was evaluated in three xenograft models of peritoneal carcinomatosis, including peritoneal mesothelioma (MSTO-211H cell line, nude mouse model),^{29,32,41} ovarian carcinoma (OVCAR-3 cell line, nude mouse model),³⁰ and PDAC-PC (Panc-1-CSC cell line, nude rat model). Peritoneal disease was established within 2–4 weeks in each model, at which point animals received 300 μL (mouse) or 1 mL (rat) injections of 0.2% HFR-eNPs 24 h prior to laparotomy and analysis. Gross examination of the peritoneal cavity using a hand-held Wood's lamp (365 nm UV light) revealed significant rhodamine fluorescence and HFR-eNP accumulation in peritoneal tumors (Figure 2).

In order to gain insight into the HFR-eNP properties responsible for tumor-specific localization, we evaluated the impact of changing material properties and surface functionality on tumoral localization. Two additional formulations were prepared and evaluated in the PDAC-PC model. First, poly(lactic-*co*-glycolic) acid nanoparticles covalently labeled with rhodamine (Rho-PLGA-NPs) were synthesized with the sodium dodecyl sulfate (SDS) surfactant used in the HFR-eNP formulation and served as a non-pH-responsive, generic polymer control possessing a similar negative ζ -potential (–40 to –50 mV). The second NP formulation was synthesized using the rhodamine-labeled eNP core material with a soy lecithin/1,2-distearoyl-*sn*-glycero-3-phosphoethanolamine-*N*-[amino(polyethylene glycol)-2000] (DSPE-PEG) (8/2 wt/wt) surfactant instead of SDS (*i.e.*, HFR-PEG-eNPs). The lecithin/DSPE-PEG surface coating reduced the ζ -potential of the particles from the –40 to –50 mV range to –12 mV.⁴²

Gross examination following IP injection in tumor-bearing animals demonstrated a lack of tumoral localization for either the Rho-PLGA-NPs or the HFR-PEG-eNPs (Figure 3). The fluorescent signal from the Rho-PLGA-NPs was detected in the peritoneal cavity but almost singly located in the ascites and peritoneal fluid with no tumoral accumulation. The HFR-PEG-eNPs appeared to be completely absent from the peritoneal cavity, consistent with the PEG surface functionalization reducing cellular uptake and affording a more rapid clearance of the particles from the peritoneal cavity. It is unlikely that the fluorescence was quenched or bleached as the HFR-eNP formulations fluoresced vibrantly when imaged on an identical dosing/timing schedule. These findings suggest that the material properties of the eNP—pH-responsiveness, particle swelling, and surface charge—are essential components in the mechanism of tumoral localization.

Quite distinctly, no fluorescent signal was grossly observed in adjacent nontumor tissues, including the liver, spleen, intestines, stomach, and retroperitoneal organs—kidneys, adrenal gland, pancreas, and ovaries (females) (Figure 4). Likewise, no fluorescent signal was detected in the brain, heart, and lungs (Figure 4), as well as bladder (data not shown).

Because PDAC-PC presents one of the most compelling, unmet, clinical challenges and has no therapies available with “curative intent”, we conducted the remaining studies using the PDAC-PC nude rat model as a validated model system.³¹ Specifically, we determined the sensitivity and specificity of HFR-eNPs for pancreatic peritoneal tumors. Using histopathological examination as the gold standard for positive/negative identification of malignant tissues, a combination of 455 tumor nodules and different normal tissue sites from three rats were surveyed for gross visual identification of HFR-eNP fluorescence as well as histological confirmation of malignancy and fluorescence (Figure 5a). Tumor tissue sizes ranged from relatively large (>1 cm³) to sub-millimeter (~1 mm³) (Figure 5b). Of the 253 histologically confirmed tumor samples, 232 were identified by HFR-eNPs (*i.e.*, “positive”), while 21 were not (*i.e.*, “negative”). Of the 202 normal tissue samples, 200 were negative for HFR-eNP signal, while two adipose tissue areas were faintly positive. Thus, the HFR-eNP system identified IP tumors with a sensitivity of 92% (*i.e.*, true positives/all positives) and a specificity of 99% (*i.e.*, true negatives/all negatives), yielding an accuracy of 95% [*i.e.*, (true positives + true negatives)/(true positives + true negatives + false positives + false negatives)] (Table 1).

Currently, there is no sub-millimeter tumor detection imaging system for intraoperative detection of tumors to facilitate and enhance surgical resection of PDAC-PC. Other methods being investigated show promise. However, the reported success of these systems is often based upon colocalization of fluorescent probes and the bioluminescent signal from tumors, which is not detectable from sub-millimeter tumors. Additionally, the methods that exhibit high sensitivity often utilize a targeting molecule, for example, lectin-targeted avidin-FITC probes with an accuracy of 100%,⁴³ which is significant but limits the widespread applicability of the probe. The sensitivity of HFR-eNPs, which do not use targeting ligands, is comparable to these other probes. Moreover, the current technique requires only the use of an inexpensive handheld Wood’s UV lamp already commonly found in surgical suites.

Examination of the particle distribution in the current study reveals that the HFR-eNPs accumulated in peritoneal tumors with high specificity, even if situated adjacent to normal tissues, such as kidney, intestine, pancreas, liver, spleen, stomach, large and small intestines (gut), adipose tissue, and blood vessels with nearly complete sparing of nontumor tissues (Figure 5a). This high specificity is likely due to four tumor-specific biological factors dictating penetration and accumulation of HFR-eNPs based on the latter’s biophysical properties.

First, the density of HFR-eNPs is greatest at the tumor surface layer with signal intensity decreasing with depth in most cases (Figure 5a), suggesting tumor penetration from the surface. This observation is consistent with the absence of HFR-eNP accumulation in the microvasculature (Figure 6a) and in vessel wall layers (Figure 6b) despite proximity to eNP+ tumor cells, as well as absence in highly vascularized organ tissues—brain, heart, kidney, liver, and spleen (Figure 4). Notably, analysis of the mesothelial lining of the peritoneal cavity did not exhibit fluorescence, indicating nonpenetration and/or nonaccumulation of HFR-eNPs in normal peritoneal mesothelium. This could be due to negative-charge repulsion because both the normal mesothelial glycocalyx and HFR-eNPs are net negatively charged. As the likelihood of tumor localization through the vasculature is remote, the data

suggest that HFR-eNPs likely penetrate tumors from the tumor surface through aberrant peri-tumoral mesothelial cells and not *via* the circulation (Figure 6a,b).

Second, HFR-eNP fluorescence throughout sub-millimeter peritoneal tumors is frequently complete in contrast to larger tumors, consistent with time-dependent penetration and accumulation. Alternatively, potential impedance by dense stromal collagen fibers present in larger PDAC-PC tumors could slow radial penetration, though complete radial penetration has been observed previously.²⁰

Third, biological factors underlying tumor-specific accumulation of eNPs in intraperitoneal tumors likely include rapid uptake of nanoparticles by metabolically active cancer cells as seen for peritoneal mesothelioma tumors⁴¹ and consistent with the increased endocytosis of tumor cells.⁴⁴ This deduction is supported by the detection of HFR-eNPs within cells rather than distributed in the extracellular matrix surrounding tumor cells (Figure 6a). This is consistent with previous findings that eNPs can deliver therapeutics specifically to tumor cells while sparing normal tissues.²⁰ Moreover, these results are consistent with our previously published findings in an identical model of PDAC-PC demonstrating time-dependent eNP accumulation, wherein 1 h after injection the fluorescent eNPs were still in the peritoneal fluid and not localized to tumors; in contrast, 4 h after injection, tumor localization was significant with negligible particle fluorescence in the peritoneal fluid.³¹ By 24 h, tumor localization was prominent with no residual fluorescence in the peritoneal fluid.³¹

Fourth, due to the pH-responsive swelling functionality, where HFR-eNPs expand from ~30 to ~500 nm—described in detail in ref 45 and in refs 29, 31, 36, 42, and 46—the pH of the local microenvironment may play a role in the specificity of the HFR-eNPs for tumors. To determine the relationship of eNP localization and low-pH tumor microenvironments, we immunostained tissues for (1) HIF1 α as an indicator of cellular hypoxia and hypoxia-associated low pH and (2) lactate dehydrogenase-A (LDH-A) expression as an indicator of low-pH tumor microenvironments from the production of lactic acid. We used fluorescently labeled human-specific anti-HIF1 α and anti-LDH-A antibodies to ensure fluorescence would be specific to the human-derived Panc-1 CSC tumor cells. Notably, immunostaining of HFR-eNP-treated tumor sections revealed a preference for localization to regions with human-specific HIF1 α -positive cells (Figure 6c), albeit not all HIF1 α tumor cells. Hypoxia of microscopic tumors is consistent with literature reports of hypoxia in sub-millimeter tumors prior to the angiogenic switch, tumor vascularization, and growth.⁴⁷ HFR-eNP localization to HIF1 α -positive, hypoxic, low-pH tumor regions is also consistent with the pH-responsive expansile swelling property.^{36,41,45} Additionally, HFR-eNPs localized to LDH-A-positive tumor cells (Figure 6d) but not all LDH-A-positive tumor cells. High expression of LDH-A, a key enzyme for glycolytic metabolism, is responsible for the increased lactate in tumors resulting in tumor acidification (pH 6.5–6.8), consistent with the Warburg effect.

Having documented high tumor-specific localization and sensitivity, we next evaluated the feasibility of using intraoperative HFR-eNP optical imaging as a guide to surgical resection of peritoneal tumors in the PDAC-PC rat model. Clinically, the 5-year survival of resectable

PDAC-PC has remained stagnant at 20–21% for decades despite significant improvements in 30-day postoperative mortality;¹⁶ this stagnation may be attributed to the inability to remove sub-millimeter microtumors as macroscopic tumors >1 cm³ are more easily identified and resected.¹⁷ The detection of microtumors intraoperatively would enable removal of microtumors along with the macrotumors deemed resectable. Using identical protocols for optical imaging described above, three animals were xenografted and the tumors allowed to establish for 2 weeks. HFR-eNPs were injected IP, and 24 h later, animals were anesthetized and underwent laparotomy to evaluate the potential for HFR-eNP image-guided surgical resection of peritoneal tumors, especially sub-millimeter tumors. Simulating an intraoperative scenario, we imaged peritoneal tumors with a hand-held long-wave UV lamp, resected, and reimaged post-resection.

Figure 7 reveals a significant reduction in fluorescent signal following resection, demonstrating the feasibility of intraoperative fluorescence-guided resection. Given that sub-millimeter peritoneal tumors are detected with high sensitivity and specificity, pilot observations suggest a potential image-guided surgical resection paradigm for sub-millimeter tumors, which are not detectable with current technologies. Although further evaluation is needed to determine the efficacy of HFR-eNP-guided resections, these studies suggest that the addition of an HFR-eNP probe to the surgical oncologist's toolkit may prove invaluable in (1) detecting and, hence, removing occult sub-millimeter PDAC-PC tumors in resectable PDAC patients in order to improve patient survival; (2) potentially overcoming the current nonefficacy of cytoreductive surgery for PDAC-PC; and (3) potentially reducing recurrence after cytoreductive surgery in ovarian, gastric, colorectal, and mesothelioma peritoneal carcinomatosis.

CONCLUSION

A series of fluorescent HFR-eNP probes possessing varying concentrations of rhodamine are synthesized and characterized by SEM, DLS, and for their fluorescent properties. The HFR-eNPs localize to *in vivo* peritoneal tumors of mesothelioma, ovarian, and pancreatic origin after intraperitoneal injection and are easily visualized using an inexpensive hand-held long-wave UV lamp. Tumor localization is dependent on eNP composition and surface functionality as similar negatively charged PLGA-NPs or PEGylated HFR-PEG-eNPs do not accumulate in tumors. Using the *in vivo* pancreatic xenograft model, HFR-eNPs detect tumors intraoperatively with 95% accuracy. Importantly, sub-millimeter tumors are identified as well as more readily observable sub-centimeter tumors. HFR-eNPs home to tumor regions with high expression of LDH-A and hypoxic areas with high expression of HIF1 α . A pilot fluorescently guided cytoreductive surgery of Panc-1 tumors in a xenograft rat model shows proof-of-principle feasibility for using HFR-eNPs as intraoperative probes for guiding resections. Success of this facile, simple, intraoperative visualization method may prove useful in increasing detection and, subsequently, resection of sub-millimeter tumors. Continued development and evaluation of nano-based intraoperative visual aids for surgical resections will have a direct impact on clinical care.

METHODS

HFR-eNP Synthesis

The highly fluorescent rhodamine-labeled expansile nanoparticles (HFR-eNPs) were synthesized utilizing a previously reported miniemulsion technique.³⁶ The organic phase (500 μL dichloromethane) contained 50 mg of monomer (5-methyl-2-(2,4,6-trimethoxyphenyl)-[1,3]-5-dioxanylmethyl methacrylate), 0.5 mg of cross-linker (1,4-*O*-methacryloylhydroquinone), and either 0.02, 0.2, or 2.0 % wt/wt (monomer/rhodamine) of methacryloxyethyl thiocarbamoyl rhodamine B (Rho, Polysciences, Inc., Warrington, PA). The aqueous phase (2 mL 10 mM pH 7.4 phosphate buffer) contained 16 mg of SDS (Sigma-Aldrich, St. Louis, MO) as a surfactant. Immediately after the aqueous phase was added to the organic phase, the solution was placed under argon atmosphere, sonicated for 10 min (1 s pulses with 2 s delays), and then 20 μL of 200 mM ammonium persulfate and 2 μL of *N,N,N',N'*-tetramethylethylenediamine were added to initiate the polymerization *in situ*. The solution was then stirred under argon for 2 h and under air overnight. The resulting nanoparticles were dialyzed in 5 mM pH 7.4 phosphate buffer for 24 h and kept within dark containers to preserve fluorescent properties until further characterization.

HFR-eNP Characterization

The diameter and surface charge of the HFR-eNPs were measured using a Brookhaven DLS (Brookhaven Instruments Corp.) with ZetaPALS ζ -potential analyzer. Particles were diluted 100 \times in deionized water prior to measurement. The morphology and size distribution were analyzed *via* SEM using a Zeiss SUPRA 40VP. Samples for SEM were prepared by diluting HFR-eNPs 1:1000 in deionized water and adding 10 μL of this dilution onto silicon wafers, which were allowed to dry. The wafers were subsequently affixed with copper tape to aluminum sample stubs. The samples were further coated with \sim 5 nm of Au/Pd before imaging.

The fluorescence spectra of the HFR-eNPs were measured using a Photon Technology International (PTI) fluorometer, and the absorption spectra were measured using an HP 8453 UV-visible spectrophotometer. The fluorescence emission spectra of the particles or free rhodamine were also evaluated in aqueous (*e.g.*, deionized water, 10 mM pH 5 acetate buffer, or 10 mM pH 7.4 phosphate buffer) as well as organic solvent (*e.g.*, dichloromethane, ethyl acetate) conditions.

The density of the particles was calculated by lyophilizing the HFR-eNPs, recording the mass, and then adding an exact amount (either 5 or 10 mL) of water to the particles. This solution was placed in a volumetric flask appropriate for the added amount of water, and the excess solution was removed and precisely measured with a micropipette to determine the volume of displaced liquid and, thus, the density of the particles.

Cell Culture and *In Vitro* Cell Viability Assay

Panc1 cells (ATCC) were maintained at 37 $^{\circ}\text{C}$ under 5% CO_2 using DMEM media containing 10% fetal bovine serum and 1% glutamine–penicillin–streptomycin. HFR-eNP cytotoxicity was evaluated using an MTS assay (CellTiter 96 Aqueous One, Promega,

Madison, WI). Briefly, Panc1 cells were cultured in a 96-well plate at 3000 cells/well for 1 day, after which the medium was exchanged for media containing either no treatment or 0.02, 0.2, or 2.0% HFR-eNPs. The cells were incubated with treatment for 3 days, after which cell viability was quantified relative to the no treatment control, after correcting for background absorbance. Two wells per treatment concentration were used, and the assay was repeated three times.

***In Vivo* Murine Mesothelioma and Ovarian Tumor Models**

Previously developed murine models of established mesothelioma and ovarian cancer were employed.^{30,41} Briefly, 6–8 week old, female, athymic, nude (NU/J) mice from Jackson Laboratory were housed under sterile conditions. Animal care and procedures were conducted with Institutional Animal Care and Use Committee approval, in strict compliance with all federal and institutional guidelines for the care and use of laboratory animals (Dana-Farber Cancer Institute, Boston, MA). Mice received intraperitoneal injections of 5×10^6 MSTO-211H or 1×10^6 OVCAR-3 cells, yielding established tumors within 2–4 weeks.

***In Vivo* Rat Pancreatic Tumor Model Using CSCs**

A previously developed rat model of pancreatic cancer was used for this study with all work performed in accordance with BUSM institutional guidelines.³¹ Briefly, Panc-1 cells were harvested in log phase and subcultured in complete MammoCult medium (Stem Cell Technologies, BC, Canada) in 5% CO₂ in a humidified incubator at 37 °C. After 2–3 weeks in culture, Panc-1 cells were harvested and plated in complete MammoCult medium containing 0.5% methylcellulose (Stem Cell Technologies, BC, Canada) in 100 mm ultralow attachment plates. Peritoneal tumors were developed from septenary CSCs. The Panc-1-CSC-derived peritoneal tumor model was developed in 4–5 week-old nude^{nu/nu} female rats (Charles River Laboratories, MA). The intraperitoneal tumor implantation was performed in anesthetized animals using isoflurane maintained at 1–1.5%. Intraperitoneal injection of 2×10^6 CSCs suspended in 1 mL of M2 media was performed under sterile conditions.

***In Vivo* Localization of HFR-eNPs to PPC Tumors**

Animal studies were performed in accordance with Dana-Farber Cancer Institute and BUSM institutional guidelines. At designated time points after tumor initiation (2 weeks for mesothelioma, 4 weeks for ovarian, 3 weeks for pancreatic), HFR-eNPs were injected intraperitoneally under sterile conditions with animals under isoflurane anesthesia and aseptic preparation of the injection site. Animals received injections of 300 μ L (mice) or 1 mL (rats) of HFR-eNPs (25 mg polymer/mL). Fluorescent imaging was performed 24 h after HFR-eNP injection using a hand-held Woods lamp unless otherwise specified.

Intraoperative visualization of HFR-eNP localization was performed following midline abdominal incision and retraction under isoflurane anesthesia in sterile conditions. A Woods lamp (long-wave UV) was used to excite the rhodamine and fluorescence was documented with a digital camera. *Ex vivo* fluorescence imaging was also performed using the Woods lamp and digital photography of tumors and whole organs as well as the organs cut and laid open-face.

Immunohistochemistry and Staining of Tissues

Direct immunostaining for LDH-A and HIF1 α was performed on serial tumor tissue sections prepared from tumors isolated from xenografted rats. Tumors were fixed in 4% paraformaldehyde (pH 7.4), followed by routine histology processing and paraffin embedding. Tissue sections (4–5 μm) were then processed for staining with routine deparaffinization, dehydration, rehydration, followed by antigen retrieval. After washes, treatment with FX Signal Enhance (Invitrogen) and blocking with 1% BSA, AlexaFluor (AF)-labeled primary antibodies (50 $\mu\text{g}/\text{mL}$ of anti-LDH-A and anti-HIF1 α) were added and incubated in a humidified chamber at 4 °C for 16 h. Thereafter, slides were rinsed and mounted with Prolong Diamond antifade mountant with DAPI (Invitrogen) and sealed after 24 h. The APEX AF labeling kit was used according to manufacturer's specifications (Invitrogen) to label mouse monoclonal anti-human HIF1 α antibody (Creative Diagnostics) and the mouse monoclonal antilactate dehydrogenase-A antibody (Abcam) with either AF488 or AF568 as needed. For immunostaining and co-immunostaining, 50 $\mu\text{g}/\text{mL}$ of labeled anti-HIF1 α and anti-LDH-A antibodies was used.

Intraoperative Image-Guided Resection of Sub-millimeter Pancreatic Tumors via Fluorescent Nanoparticle Probes

Using identical protocols for optical imaging described above, three animals were xenografted and the tumors allowed to establish for 2 weeks. HFR-eNPs were injected IP and, 24 h later, animals were anesthetized using isoflurane and underwent laparotomy in sterile manner to evaluate the potential for HFR-eNP image-guided surgical resection/elimination of peritoneal tumors, especially sub-millimeter tumors. Simulating an intraoperative scenario, we imaged peritoneal tumors with a hand-held long-wave UV lamp, resected, and then reimaged post-resection. Resection of sub-millimeter tumors was first performed in the omentum, followed by tumors on the intestinal mesentery, then over retroperitoneal organs—kidney, ovaries, and uterine horns. Excessive bleeding was not observed.

Supplementary Material

Refer to Web version on PubMed Central for supplementary material.

Acknowledgments

The authors would like to acknowledge funding support for this project from The Boston University Nanotechnology Innovation Center (BU nano), the Cross-Disciplinary Training in Nanotechnology for Cancer (XTNC NIH R25 CA153955) Training Fellowship, the Biomaterials Training Fellowship (NIH T32 EB006359), the NIH Small Business Innovation Research program (R43CA189215-01), Boston University, and Boston University School of Medicine.

References

1. Ghosh D, Bagley AF, Na YJ, Birrer MJ, Bhatia SN, Belcher AM. Deep, Noninvasive Imaging and Surgical Guidance of Submillimeter Tumors Using Targeted M13-Stabilized Single-Walled Carbon Nanotubes. *Proc Natl Acad Sci U S A*. 2014; 111:13948–13953. [PubMed: 25214538]
2. Metildi CA, Kaushal S, Hardamon CR, Snyder CS, Pu M, Messer KS, Talamini MA, Hoffman RM, Bouvet M. Fluorescence-Guided Surgery Allows for More Complete Resection of Pancreatic

- Cancer, Resulting in Longer Disease-Free Survival Compared with Standard Surgery in Orthotopic Mouse Models. *J Am Coll Surg.* 2012; 215:126–35. discussion 135–136. [PubMed: 22632917]
3. van Dam GM, Themelis G, Crane LMA, Harlaar NJ, Pleijhuis RG, Kelder W, Sarantopoulos A, de Jong JS, Arts HJG, van der Zee AGJ, Bart J, Low PS, Ntziachristos V. Intraoperative Tumor-Specific Fluorescence Imaging in Ovarian Cancer by Folate Receptor-A Targeting: First in-Human Results. *Nat Med.* 2011; 17:1315–1319. [PubMed: 21926976]
 4. Houghton JL, Zeglis BM, Abdel-Atti D, Aggeler R, Sawada R, Agnew BJ, Scholz WW, Lewis JS. Site-Specifically Labeled Ca19.9-Targeted Immunoconjugates for the Pet, Nirx, and Multimodal Pet/Nirx Imaging of Pancreatic Cancer. *Proc Natl Acad Sci U S A.* 2015; 112:15850–15855. [PubMed: 26668398]
 5. Gilmore DM, Khullar OV, Gioux S, Stockdale A, Frangioni JV, Colson YL, Russell SE. Effective Low-Dose Escalation of Indocyanine Green for near-Infrared Fluorescent Sentinel Lymph Node Mapping in Melanoma. *Ann Surg Oncol.* 2013; 20:2357–2363. [PubMed: 23440551]
 6. Chen S, Yu G, Zhang B, Wang Y, Zhang N, Chen Y. Human Serum Albumin (Hsa) Coated Liposomal Indocyanine Green for in Vivo Tumor Imaging. *RSC Adv.* 2016; 6:15220–15225.
 7. Hill TK, Abdulahad A, Kelkar SS, Marini FC, Long TE, Provenzale JM, Mohs AM. Indocyanine Green-Loaded Nanoparticles for Image-Guided Tumor Surgery. *Bioconjugate Chem.* 2015; 26:294–303.
 8. Lee S, Xie J, Chen X. Activatable Molecular Probes for Cancer Imaging. *Curr Top Med Chem.* 2010; 10:1135–1144. [PubMed: 20388112]
 9. Liu F, Deng D, Chen X, Qian Z, Achilefu S, Gu Y. Folate-Polyethylene Glycol Conjugated near-Infrared Fluorescence Probe with High Targeting Affinity and Sensitivity for in Vivo Early Tumor Diagnosis. *Mol Imaging Biol.* 2010; 12:595–607. [PubMed: 20376571]
 10. De Jesus E, Keating JJ, Kularatne SA, Jiang J, Judy R, Predina J, Nie S, Low P, Singhal S. Comparison of Folate Receptor Targeted Optical Contrast Agents for Intraoperative Molecular Imaging. *Int J Mol Imaging.* 2015; 2015:469047. [PubMed: 26491562]
 11. Dang X, Gu L, Qi J, Correa S, Zhang G, Belcher AM, Hammond PT. Layer-by-Layer Assembled Fluorescent Probes in the Second near-Infrared Window for Systemic Delivery and Detection of Ovarian Cancer. *Proc Natl Acad Sci U S A.* 2016; 113:5179–5184. [PubMed: 27114520]
 12. Fang M, Peng CW, Pang DW, Li Y. Quantum Dots for Cancer Research: Current Status, Remaining Issues, and Future Perspectives. *Cancer Biol Med.* 2012; 9:151–163. [PubMed: 23691472]
 13. Li Y, Li Z, Wang X, Liu F, Cheng Y, Zhang B, Shi D. In Vivo Cancer Targeting and Imaging-Guided Surgery with near Infrared-Emitting Quantum Dot Bioconjugates. *Theranostics.* 2012; 2:769–776. [PubMed: 22916076]
 14. Nie L, Chen M, Sun X, Rong P, Zheng N, Chen X. Palladium Nanosheets as Highly Stable and Effective Contrast Agents for in Vivo Photoacoustic Molecular Imaging. *Nanoscale.* 2014; 6:1271–1276. [PubMed: 24317132]
 15. Cruz-Monserrate Z, Roland CL, Deng D, Arumugam T, Moshnikova A, Andreev OA, Reshetnyak YK, Logsdon CD. Targeting Pancreatic Ductal Adenocarcinoma Acidic Microenvironment. *Sci Rep.* 2014; 4:4410. [PubMed: 24642931]
 16. Thomassen I, Lemmens VE, Nienhuijs SW, Luyer MD, Klaver YL, de Hingh IH. Incidence, Prognosis, and Possible Treatment Strategies of Peritoneal Carcinomatosis of Pancreatic Origin: A Population-Based Study. *Pancreas.* 2013; 42:72–75. [PubMed: 22850624]
 17. Gottlieb S. Resectable Pancreatic Cancer Needs Surgery, Then Chemotherapy. *Br Med J.* 2004; 328:661–661. [PubMed: 15031222]
 18. Gnerlich JL, Luka SR, Deshpande AD, Dubray BJ, Weir JS, Carpenter DH, Brunt EM, Strasberg SM, Hawkins WG, Linehan DC. Microscopic Margins and Patterns of Treatment Failure in Resected Pancreatic Adenocarcinoma. *Arch Surg.* 2012; 147:753–760. [PubMed: 22911074]
 19. Van den Broeck A, Sergeant G, Ectors N, Van Steenberghe W, Aerts R, Topal B. Patterns of Recurrence after Curative Resection of Pancreatic Ductal Adenocarcinoma. *Eur J Surg Oncol.* 2009; 35:600–604. [PubMed: 19131205]

20. Sodek KL, Murphy KJ, Brown TJ, Ringuette MJ. Cell-Cell and Cell-Matrix Dynamics in Intraperitoneal Cancer Metastasis. *Cancer Metastasis Rev.* 2012; 31:397–414. [PubMed: 22527451]
21. Tarin D, Price JE, Kettlewell MG, Souter RG, Vass AC, Crossley B. Mechanisms of Human Tumor Metastasis Studied in Patients with Peritoneovenous Shunts. *Cancer Res.* 1984; 44:3584–3592. [PubMed: 6744281]
22. Sugarbaker PH. Surgical Management of Carcinomatosis from Colorectal Cancer. *Clin Colon Rectal Surg.* 2005; 18:190–203. [PubMed: 20011302]
23. Piso P, Dahlke MH, Loss M, Schlitt HJ. Cytoreductive Surgery and Hyperthermic Intraperitoneal Chemotherapy in Peritoneal Carcinomatosis from Ovarian Cancer. *World J Surg Oncol.* 2004; 2:21–21. [PubMed: 15222884]
24. Yan TD, Deraco M, Baratti D, Kusamura S, Elias D, Glehen O, Gilly FN, Levine EA, Shen P, Mohamed F, Moran BJ, Morris DL, Chua TC, Piso P, Sugarbaker PH. Cytoreductive Surgery and Hyperthermic Intraperitoneal Chemotherapy for Malignant Peritoneal Mesothelioma: Multi-Institutional Experience. *J Clin Oncol.* 2009; 27:6237–6242. [PubMed: 19917862]
25. Dhingra VK, Mahajan A, Basu S. Emerging Clinical Applications of Pet Based Molecular Imaging in Oncology: The Promising Future Potential for Evolving Personalized Cancer Care. *Indian J Radiol Imaging.* 2015; 25:332–341. [PubMed: 26752813]
26. Zeng C, Shang W, Wang K, Chi C, Jia X, Fang C, Yang D, Ye J, Fang C, Tian J. Intraoperative Identification of Liver Cancer Microfoci Using a Targeted near-Infrared Fluorescent Probe for Imaging-Guided Surgery. *Sci Rep.* 2016; 6:21959. [PubMed: 26923919]
27. Gioux S, Choi HS, Frangioni JV. Image-Guided Surgery Using Invisible near-Infrared Light: Fundamentals of Clinical Translation. *Mol Imaging.* 2010; 9:237–255. [PubMed: 20868625]
28. Wilhelm S, Tavares AJ, Dai Q, Ohta S, Audet J, Dvorak HF, Chan WCW. Analysis of Nanoparticle Delivery to Tumours. *Nat Rev Mater.* 2016; 1:16014.
29. Colson YL, Liu R, Southard EB, Schulz MD, Wade JE, Griset AP, Zubris KA, Padera RF, Grinstaff MW. The Performance of Expansile Nanoparticles in a Murine Model of Peritoneal Carcinomatosis. *Biomaterials.* 2011; 32:832–840. [PubMed: 21044799]
30. Gilmore MD, Schulz MM, Liu MR PhD, Zubris PKAV, Padera MRF, Catalano SPJ, Grinstaff PMW, Colson MYL PhD. Cytoreductive Surgery and Intraoperative Administration of Paclitaxel-Loaded Expansile Nanoparticles Delay Tumor Recurrence in Ovarian Carcinoma. *Ann Surg Oncol.* 2013; 20:1684–1693. [PubMed: 23128939]
31. Herrera VL, Colby AH, Tan GA, Moran AM, O'Brien MJ, Colson YL, Ruiz-Opazo N, Grinstaff MW. Evaluation of Expansile Nanoparticle Tumor Localization and Efficacy in a Cancer Stem Cell-Derived Model of Pancreatic Peritoneal Carcinomatosis. *Nanomedicine (London, U K).* 2016; 11:1001–1015.
32. Colby AH, Liu R, Schulz MD, Padera RF, Colson YL, Grinstaff MW. Two-Step Delivery: Exploiting the Partition Coefficient Concept to Increase Intratumoral Paclitaxel Concentrations in Vivo Using Responsive Nanoparticles. *Sci Rep.* 2016; 6:18720. [PubMed: 26740245]
33. Eldridge, J., Colby, AH., Willmott, GR., Yu, S., Grinstaff, MW. Use of Tunable Pores for Accurate Characterization of Micro- & Nano-Particle Systems in Nanomedicine. In: Chang, TMS., editor. *Selected Topics in Nanomedicine.* World Scientific; Hackensack, NJ: 2012. p. 219-255.
34. Liu R, Gilmore DM, Zubris KA, Xu X, Catalano PJ, Padera RF, Grinstaff MW, Colson YL. Prevention of Nodal Metastases in Breast Cancer Following the Lymphatic Migration of Paclitaxel-Loaded Expansile Nanoparticles. *Biomaterials.* 2013; 34:1810–1819. [PubMed: 23228419]
35. Zubris KA, Liu R, Colby A, Schulz MD, Colson YL, Grinstaff MW. In Vitro Activity of Paclitaxel-Loaded Polymeric Expansile Nanoparticles in Breast Cancer Cells. *Biomacromolecules.* 2013; 14:2074–2082. [PubMed: 23617223]
36. Griset AP, Walpole J, Liu R, Gaffey A, Colson YL, Grinstaff MW. Expansile Nanoparticles: Synthesis, Characterization, and *in Vivo* Efficacy of an Acid-Responsive Polymeric Drug Delivery System. *J Am Chem Soc.* 2009; 131:2469–2471. [PubMed: 19182897]
37. Wang X, Xu S, Xu W. Luminescent Properties of Dye-Pmma Composite Nanospheres. *Phys Chem Chem Phys.* 2011; 13:1560–1567. [PubMed: 21103543]

38. Larson DR, Ow H, Vishwasrao HD, Heikal AA, Wiesner U, Webb WW. Silica Nanoparticle Architecture Determines Radiative Properties of Encapsulated Fluorophores. *Chem Mater*. 2008; 20:2677–2684.
39. Fikry M, Omar MM, Ismail LZ. Effect of Host Medium on the Fluorescence Emission Intensity of Rhodamine B in Liquid and Solid Phase. *J Fluoresc*. 2009; 19:741–746. [PubMed: 19221868]
40. Casey KG, Quitevis EL. Effect of Solvent Polarity on Nonradiative Processes in Xanthene Dyes: Rhodamine B in Normal Alcohols. *J Phys Chem*. 1988; 92:6590–6594.
41. Liu R, Colby AH, Gilmore D, Schulz M, Zeng J, Padera RF, Shirihai O, Grinstaff MW, Colson YL. Nanoparticle Tumor Localization, Disruption of Autophagosomal Trafficking, and Prolonged Drug Delivery Improve Survival in Peritoneal Mesothelioma. *Biomaterials*. 2016; 102:175–86. [PubMed: 27343465]
42. Stolzoff M, Ekladios I, Colby AH, Colson YL, Porter TM, Grinstaff MW. Synthesis and Characterization of Hybrid Polymer/Lipid Expansile Nanoparticles: Imparting Surface Functionality for Targeting and Stability. *Biomacromolecules*. 2015; 16:1958–1966. [PubMed: 26053219]
43. Hama Y, Urano Y, Koyama Y, Kamiya M, Bernardo M, Paik RS, Krishna MC, Choyke PL, Kobayashi H. In Vivo Spectral Fluorescence Imaging of Submillimeter Peritoneal Cancer Implants Using a Lectin-Targeted Optical Agent. *Neoplasia*. 2006; 8:607–612. [PubMed: 16867223]
44. Mosesson Y, Mills GB, Yarden Y. Derailed Endocytosis: An Emerging Feature of Cancer. *Nat Rev Cancer*. 2008; 8:835–850. [PubMed: 18948996]
45. Colby AH, Colson YL, Grinstaff MW. Microscopy and Tunable Resistive Pulse Sensing Characterization of the Swelling of Ph-Responsive, Polymeric Expansile Nanoparticles. *Nanoscale*. 2013; 5:3496–3504. [PubMed: 23487041]
46. Zubris KAV, Colson YL, Grinstaff MW. Hydrogels as Intracellular Depots for Drug Delivery. *Mol Pharmaceutics*. 2012; 9:196–200.
47. Li XF, O'Donoghue JA. Hypoxia in Microscopic Tumors. *Cancer Lett*. 2008; 264:172–180. [PubMed: 18384940]

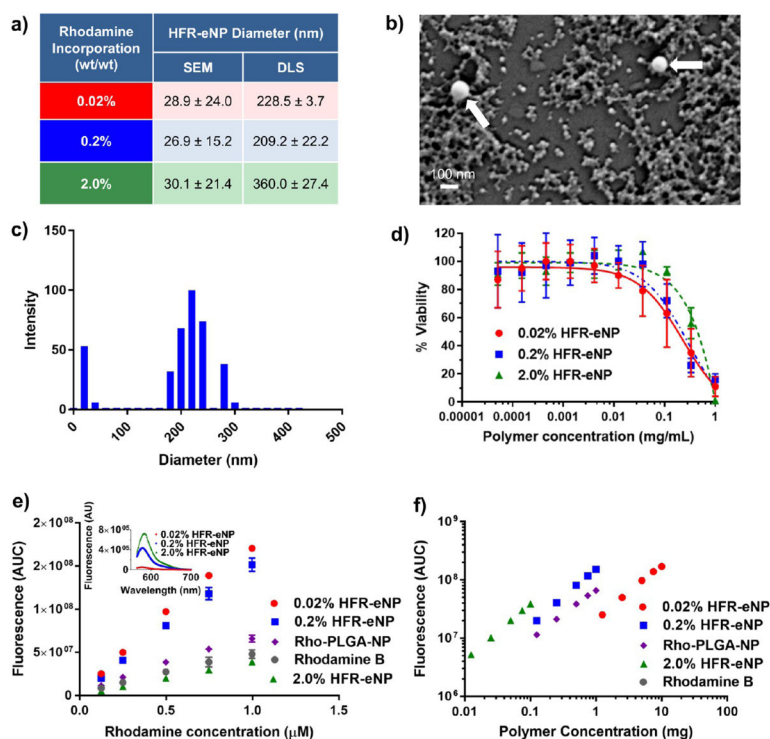


Figure 1.

Characterization of HFR-eNPs. (a) Nanoparticle diameter as a function of rhodamine incorporation as measured by SEM and DLS. (b) SEM image of 0.2% HFR-eNPs; white arrows indicate two larger particles on a background of many 20–50 nm particles. (c) Representative DLS data of 0.2% HFR-eNPs. (d) Viability of Panc-1 cells treated with HFR-eNPs as measured using an MTS assay. (e) Area under the curve (AUC) of the fluorescence emission spectra of HFR-eNPs, Rho-PLGA-NPs, and free rhodamine B as a function of rhodamine concentration in 10 mM pH 7.4 phosphate buffer. Inset: Fluorescence emission spectra of the HFR-eNPs at equivalent polymer concentrations. (f) AUC of the fluorescence emission spectra of HFR-eNPs and Rho-PLGA-NPs as a function of polymer concentration in 10 mM pH 7.4 phosphate buffer.

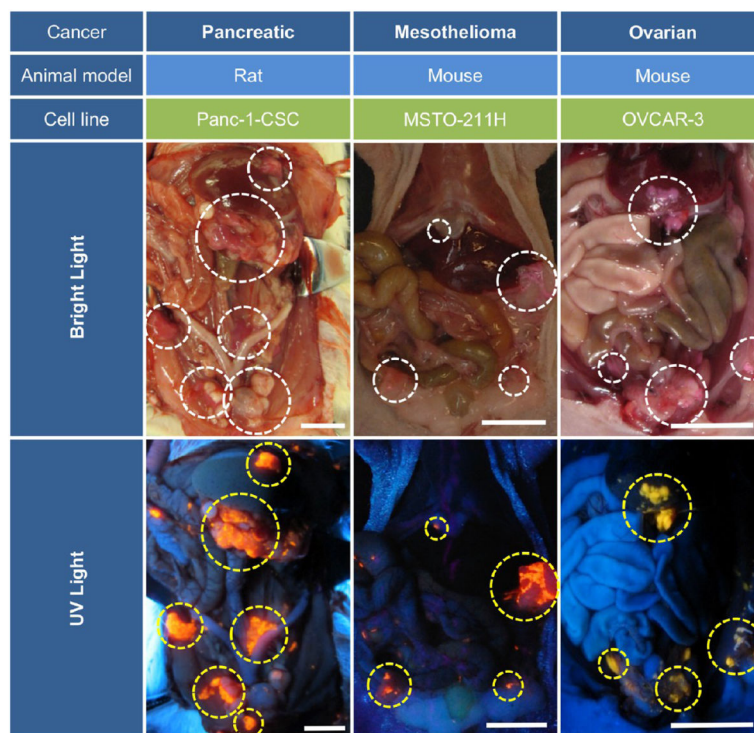


Figure 2. Highly fluorescent rhodamine-labeled expansile nanoparticles (HFR-eNPs, yellow circles in UV light images) localize to intraperitoneal tumors (white circles in bright light images) in models of pancreatic, mesothelioma, and ovarian carcinomatoses. All scale bars are 1 cm.

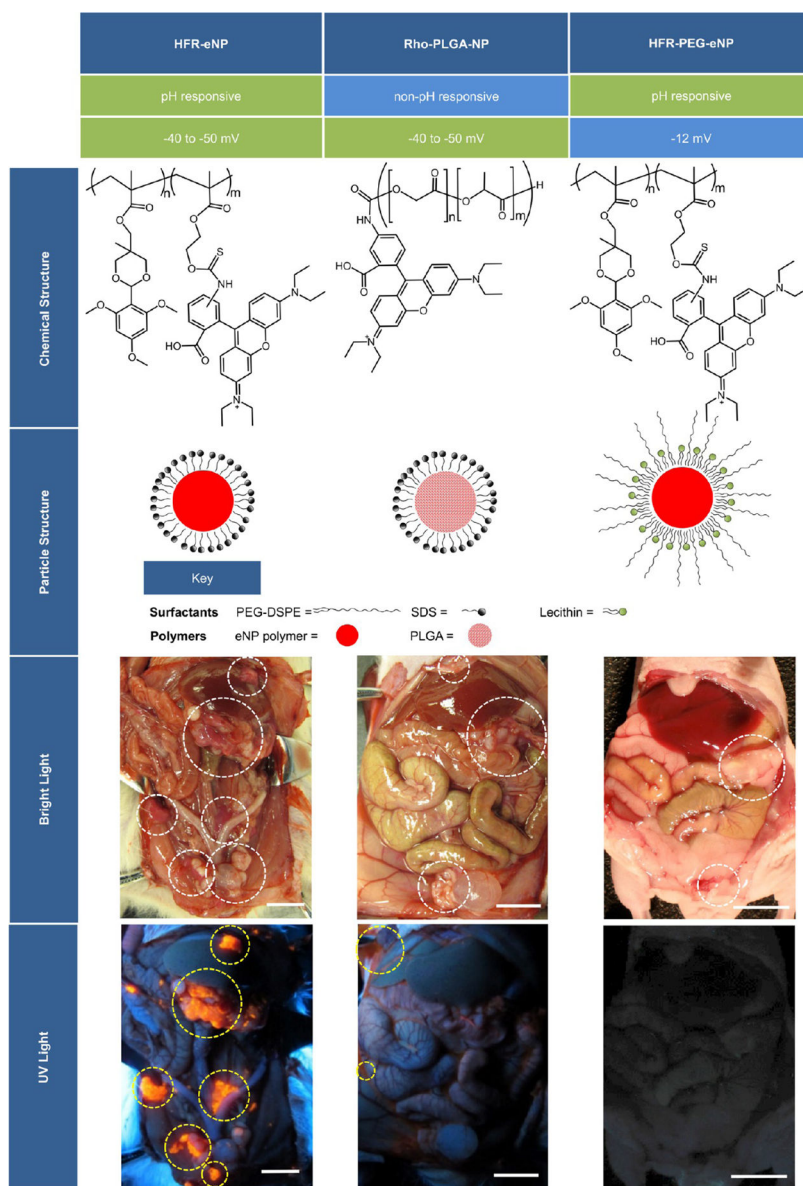


Figure 3. Comparison between three different fluorescent probes, including HFR-eNPs, Rho-PLGA-NPs, and HFR-PEG-eNPs. The Rho-PLGA-NPs have a similar effective charge but lack pH-responsive functionality, whereas the HFR-PEG-eNPs maintain the pH-responsive functionality but have a more neutral effective charge. Only the HFR-eNPs show tumor localization *in vivo*. White circles in bright light images mark regions of tumor; yellow circles in UV light images highlight regions of NP fluorescence. All scale bars are 1 cm.

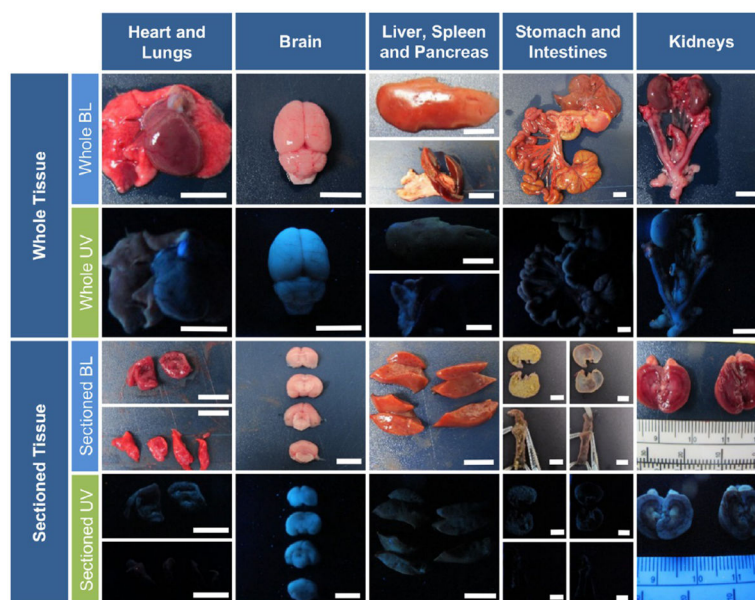


Figure 4. Visual assessment of HFR-eNP biodistribution. Representative bright light (BL) and long-wave UV light images of both whole and sectioned major organs 3 days following IP injection of 0.2% HFR-eNPs. Shown are the heart, collapsed lungs, brain, liver, spleen and pancreas, stomach with large and small intestines, mesothelium, kidneys with uterine horns, ovaries, bladder, adrenal glands, and adipose tissue. The sectioned stomach and intestine are shown with and without contents. Whole and sectioned UV images confirm nonfluorescence in these organs. All scale bars are 1 cm.

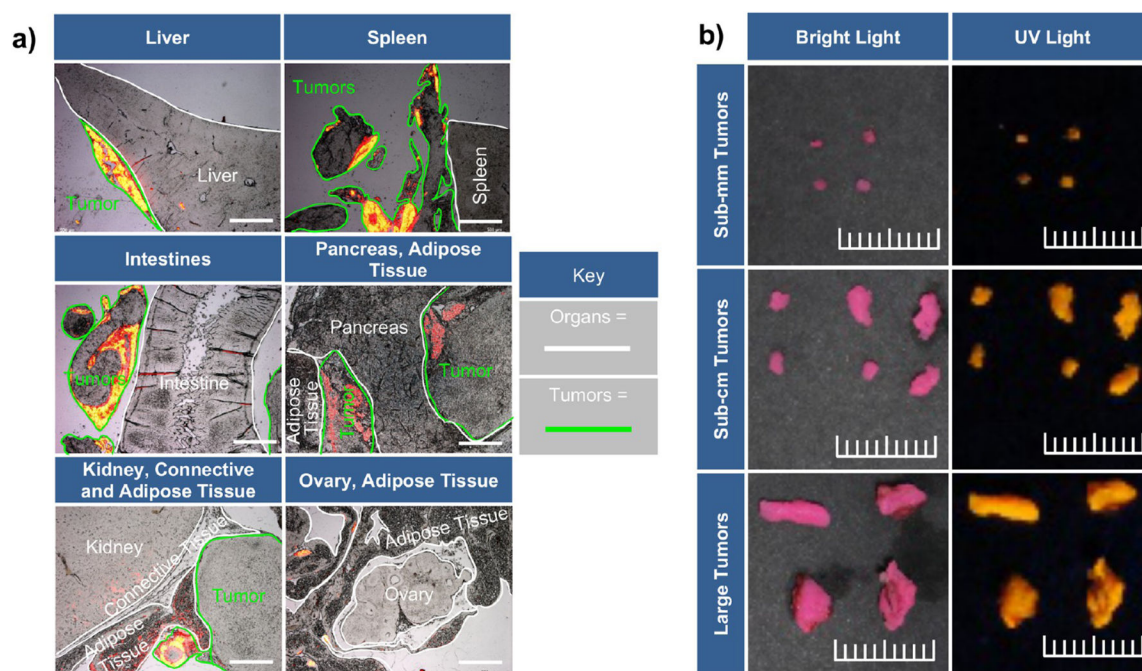


Figure 5.

Localization of HFR-eNPs to tumors. (a) Representative histological analysis using merged images of rhodamine fluorescence (yellow/orange/red color) and bright light images of tumors and adjacent normal tissues. Scale bars are 1 mm. (b) Bright light and UV images of tumors resected from a xenograft Panc1-CSC rat model. Tumors range from sub-millimeter to approximately 1 cm in size. Scale bar shows 1 cm with millimeter delineations.

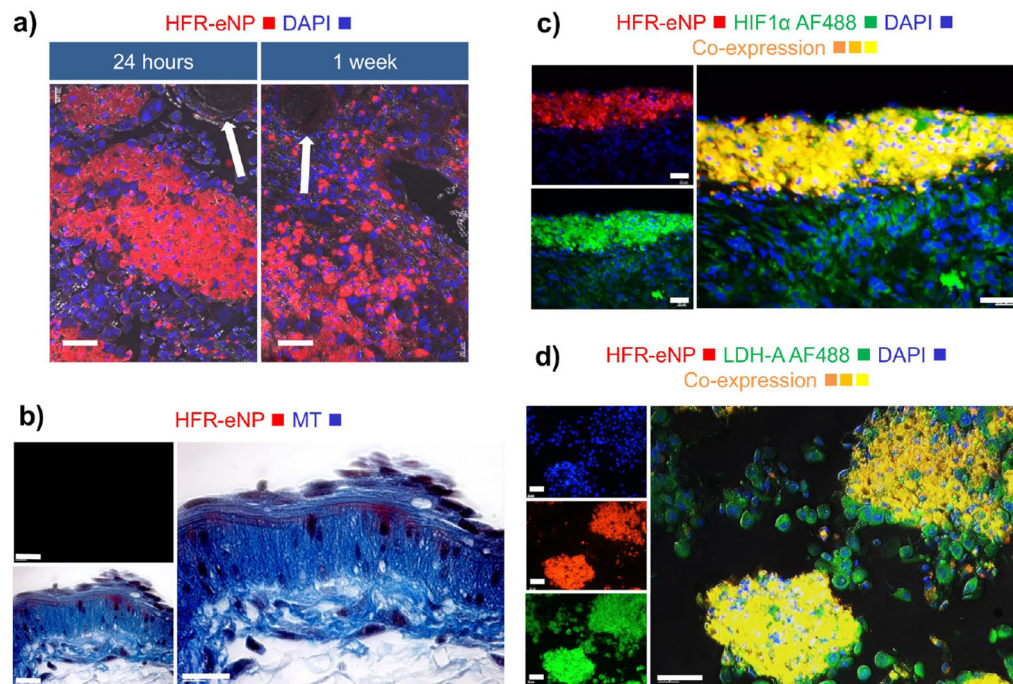


Figure 6.

Analysis of HFR-eNP localization in Panc1-CSC tumor cells. (a) HFR-eNP localization excludes blood vessels and endothelium (arrows showing blood vessel cross sections); scale bars are 40 μm . (b) Cross section of blood vessel wall showing no colocalization of HFR-eNPs; MT = Mason's Trichrome; scale bars are 20 μm . (c) Colocalization of HFR-eNPs and HIF1 α , a marker for hypoxia; scale bars are 40 μm . (d) Colocalization of HFR-eNPs and LDH-A, a marker for tumor acidification; scale bars are 40 μm .

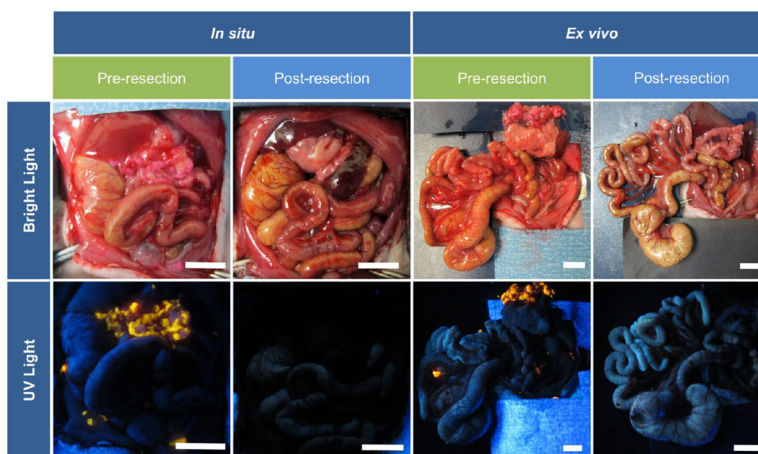


Figure 7. Demonstration of the feasibility of utilizing HFR-eNPs for cytoreductive surgery in a xenograft Panc-1-CSC rat model. Shown are bright light and corresponding UV light images revealing the presence of fluorescent tumors before, but not after, resection. The peritoneal organs are shown *in situ* as well as *ex vivo*. Scale bars are 1 cm.

Table 1Quantitative Analysis of HFR-eNP Tumoral Accumulation^a

a)		Tissue Type	
		Tumor	Normal
HFR-eNP Presence	+	232 (TP)	2 (FP)
	-	21 (FN)	200 (TN)

b)	Equation	Value
Specificity	$\frac{TN}{TN+FP}$	0.99
Sensitivity	$\frac{TP}{TP+FN}$	0.92
Accuracy	$\frac{TP+TN}{TP+TN+FP+FN}$	0.95

^aPanel a: True positives (TP), false positives (FP), true negatives (TN), and false negatives (FN) were determined by histological analysis of tissues (Figure 5a). Panel b: Specificity, sensitivity, and accuracy were determined, yielding an overall accuracy of 0.95.